Chinese Journal of Chemical Engineering 87 (2025) 239–251

Contents lists available at ScienceDirect

Chinese Journal of Chemical Engineering

journal homepage: www.elsevier.com/locate/CJChE

Full Length Article

Different rotation speeds: A novel approach to enhancing chaos and mixing efficiency in multi-shaft stirred reactors

Shuang Qin [1, 2], Tong Meng [1, 2, 3], Yu Wang [1, 2], Yundong Wang [4], Changyuan Tao [1, 2], Qian Zhang [1], Bing Li [5], Zuohua Liu [1, 2, *]

[1] *School of Chemistry and Chemical Engineering, Chongqing University, Chongqing 400044, China*
[2] *State Key Laboratory of Coal Mine Disaster Dynamics and Control, Chongqing 400044, China*
[3] *Department of Industrial Chemistry "TosoMontanari", University of Bologna, 40131 Bologna, Italy*
[4] *Department of Chemical Engineering, Tsinghua University, Beijing 100084, China*
[5] *School of Chemistry and Chemical Engineering, Yangtze Normal University, Chongqing 408100, China*

ARTICLE INFO

Article history:
Received 18 March 2025
Received in revised form 28 April 2025
Accepted 29 April 2025
Available online 3 July 2025

Keywords:
Multi-shaft stirred reactors
Rotation speeds difference
Chaos characterization
Mixing efficiency
Flow field instability

ABSTRACT

In response to the accelerating demands of industrial development, the scale-up of stirred reactors has become increasingly prevalent. Multi-shaft stirred reactors have emerged as a promising solution; however, a critical challenge remains in achieving efficient mixing while simultaneously minimizing energy consumption. Here, a novel approach based on differential rotation speeds to optimize mixing performance was proposed. Results demonstrate that a carefully configured rotation speed difference significantly enhances mixing efficiency, reducing mixing time by 17.89% and power consumption by 12.07%. This strategy not only amplifies flow field instability but also minimizes instability discrepancies, promoting a more uniform distribution of vortices across various scales. Furthermore, under this approach, the bottom impeller has the strongest impact on mixing, while the middle and lower impellers synergistically strengthen the weaker mixing regions and facilitate the redistribution of energy in the flow field. This method promotes efficient energy transfer from large-scale to small-scale vortices, ultimately improving overall mixing performance. This work offers a promising avenue for the optimal design and operation of multi-shaft stirred reactors, advancing both efficiency and energy sustainability.

1. Introduction

Mixing is a key part in industrial production in the fields of chemical, pharmaceutical, food and materials [1–8]. Stirring reactor as the core equipment directly affects the material energy transfer and reaction efficiency [9]. Although the traditional single-shaft single-impeller stirrer is simple in structure and stable in operation, it presents the interface effect triggered by chaotic mixing zone and segregation zone, which significantly restricts the mass transfer process, and there are inherent defects, such as high energy consumption and excessive motor torque. In order to cope with the current chemical industry is facing a huge challenge of increasing production demand, stirred reactors should be developed in the direction of large-scale, and in the traditional stirred reactor blindly increase its size will exacerbate the phenomena of uneven velocity gradient and rapid energy attenuation, and make it originally has the advantage of loss [10]. Furthermore, a more challenging issue is that as the flow field space expands, these reactors do not rapidly exhibit enhanced chaos and mixing instability; instead, they may lead to increased stability of the flow field, alongside new problems such as higher energy consumption and reduced equipment safety [11].

In response to the challenge of designing large-scale stirred reactors, traditional methods have been used to improve mixing performance by optimizing the structure and number of impellers: improved impeller shape to increase particle suspension efficiency in solid–liquid systems and reduce power consumption [12,13], and double helical belt and anchor impellers are designed for solid–liquid mixing in high viscosity systems [14]. Blade angle and width were also found to affect power consumption, energy efficiency and mixing time [15–17], wide blade propeller can

* Corresponding author. School of Chemistry and Chemical Engineering, Chongqing University, Chongqing 400044, China.
E-mail address: liuzuohua@cqu.edu.cn (Z. Liu).

https://doi.org/10.1016/j.cjche.2025.04.024

significantly improve energy efficiency. Flexible propeller design enhances flow field instability [18,19], and blade angles can also be adjusted between multiple propellers to suit a wide range of conditions [20–22]. However, single-shaft reactors face inherent limitations imposed by the symmetry of the flow field, and performance bottlenecks cannot be effectively overcome by structural optimization alone. This limitation becomes even more obvious under the requirement of low-carbon operation [9]. For this reason, multi-shaft mixing technology has emerged: Ascanio *et al.* [23,24] were the first to validate the enhancement effect of biaxial structure on highly viscous fluids in 2002, and Ameur [25] used multi-shaft multiple impellers for the first time for mixing non-Newtonian fluids. Subsequent studies have also investigated multi-shaft stirred reactors also exhibit outstanding performance in chaotic behavior and mixing performance [26,27]. The multi-shaft, multi-impeller structure plays an important role in enhancing energy utilization efficiency, and facilitating energy cascading across different flow field scale [28], and it has also been found that the height difference of impellers can improve mixing performance [29–31]. Multi-shaft stirred reactors have been used in some industries with high production demands. An important driver for industry for switching to multi-shaft stirred reactors is to save power draw and reducing mixing times.

However, the rotation speed has been neglected as an important operating condition for multi-shaft stirred reactors. As shown in Fig. 1, from single to multi shafts, the reactor diameter must be increased to make room for the multi-shaft impellers while keeping the liquid level low (so that the liquid volume remains constant and the ratio of height to diameter is considerably lower than unity). By reducing the height to diameter ratio (H/T) to achieve a short shaft design, stirred reactor can significantly improve the mechanical stability. Shorter stirring shafts not only reduces the risk of dynamic eccentricity caused by the long shaft deflection, but also reduces the torque requirements of the drive system. Research on single-shaft stirred reactors tends to focus on the exploration of impeller type and number of impellers, whereas multi-shaft stirred reactors have more complex and flexible design and operating conditions that allow for differentiation in height and rotation speed. On the one hand, the significant advantage of multi-shaft stirred reactors is that multiple motors can be adjusted independently. However, previous studies for multi-shaft stirred reactors have mostly used configurations with the same rotation speed for each shaft, but due to the different spatial positions of the impellers, there is obviously a difference in their effect on the fluid and their interaction with the wall, especially when there is a difference in the height. Therefore, optimization for rotation speed, by exploring their operating conditions in depth, may lead to stronger mixing performance and lower energy consumption based on existing equipment. In addition, such optimization can also reverse the motor configuration and reduce the size of motors or impellers with lower rotation speed requirements, further reducing the economic cost of the equipment. In summary, the targeted optimization of different rotation speed can not only explore the potential mixing performance of the multi-shaft stirred reactors and optimize their operating conditions, but also reveal the synergistic effect between different impellers and their specific impact on the mixing performance, which provides important support for the intelligent control of the reactor.

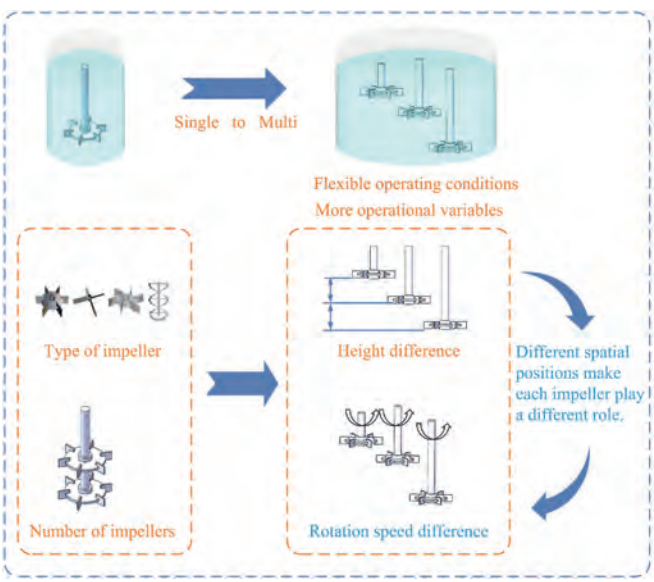

Fig. 1. Development of single and multi-shaft stirred reactors.

Computational fluid dynamics (CFD) has emerged as a critical tool for analyzing complex flow dynamics and reaction mechanisms in stirred reactors. Recent advances demonstrate its capability to resolve single-phase turbulence, solid–liquid dispersion, and energy distribution patterns [32–35], while solid-phase density and injection positioning critically affect suspension distribution [36,37]. Integration of deep learning enhances simulation robustness for mixing optimization [38]. Moreover, turbulence modeling accuracy depends on numerical schemes, with LES proving effective for characterizing unsteady flow structures in stirred tanks [39,40].

Here in, building on existing research in multi-shaft stirred reactors, this work investigates the impact of differential rotation speeds between shafts as a key factor in optimizing reactor performance. Through a combination of experimental and CFD simulations, the effects of seven different speed combinations on mixing performance, power consumption, and except for the flow field characterization which was simulated by CFD, the rest of the key parameters (including power consumption, mixing time, and chaotic characteristics) were obtained by experiment. Mixing energy, and chaotic characteristics in a three-shaft stirred system are explored, including both constant and zero speed differences. By analyzing Kolmogorov entropy, velocity distribution, turbulent kinetic energy (TKE), and turbulent dissipation rate, the influence of speed difference on flow field instability and chaotic behavior is elucidated, and the data are from experiments and CFD is only used for flow field visualization. And flow field simulations further highlight the role of speed differences in enhancing energy transfer between large-scale and small-scale vortices, thereby improving energy cascade efficiency. These findings provide a clearer understanding of the mechanisms behind enhanced mixing performance. This work emphasizes that optimizing speed configurations can facilitate more efficient redistribution of energy within the flow field, demonstrating the significant potential of this approach for achieving energy-efficient and high-performance operation in large-scale stirred reactors.

2. Experimental

2.1. Geometric model

The main research subject of this work is the three-shaft, three-impeller mixing system, with the model and dimension shown in Fig. 2 and Table S1 (in Supplementary Material). The stirred tank is a flat-bottom cylindrical tank equipped with six-blade turbine impellers made of stainless steel, with a blade thickness of 2 mm. The tank is fitted with four identical baffles, each with a width one-tenth of the tank's diameter. Pressure measurement points P1 to P5 are evenly spaced, with the same distance from the bottom and

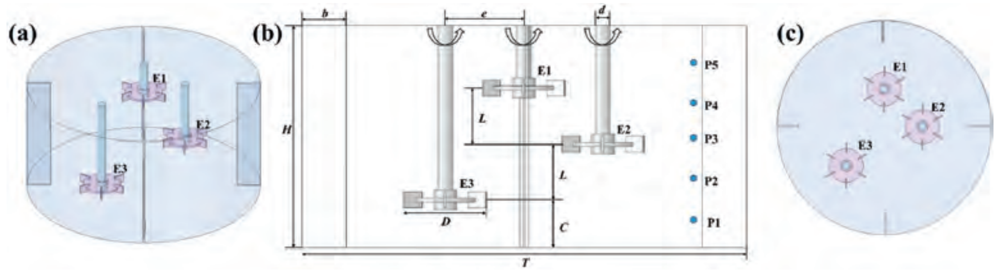

Fig. 2. Geometric model of stirred tank: (a) 3D model; (b) front view; (c) top view.

between the points. A total of seven operating conditions were set with a total rotation speed and speed difference of 600 r·min^{-1} and 50 r·min^{-1} (the speed settings were referred to the research parameters generally used by Rushton [35]) as shown in Table 1 in order to investigate the effect of speed difference on the chaotic and mixing performance.

2.2. Materials and experimental apparatus

The chemical reagents used in this work include hydrochloric acid (HCl, 1 mol·L^{-1}) and sodium hydroxide solution (NaOH, 1 mol·L^{-1}), both purchased from Aladdin Biochemistry Technology Co., Ltd. (Shanghai, China). All chemicals were used without further purification. The medium used in the experiments was distilled water, and its density and viscosity were measured using a viscometer (SNB-2, Shanghai Jingtian Electronic Instrument Co., Ltd., China). The density was $\rho = 998.2$ kg·m^{-3}, and the dynamic viscosity $\mu = 1.0 \times 10^{-3}$ Pa·s. Fig. 3 shows the main components of the experimental setup, including the stirring system and data measurement system: the drive motor and torque sensors (YSB7104, Shaoxing Wanpeng Electromechanical Co., Ltd., China), six-flat-blade turbine impeller (handmade), baffles (handmade), acrylic stirring tank (handmade), pressure sensors (AE-S, Nanjing Aier Sensing Technology Co., Ltd., China. Sampling frequency 1000 Hz), and camera (EOS 80D, Canon, China).

2.3. Experimental method

In this work, the speed settings for all operating conditions range from 150 to 250 r·min^{-1}. Since the rotation speeds of the three impellers in this setup are not the same, the Reynolds number (*Re*) is calculated for all speeds of 150 r·min^{-1}. According to Eq. (1), the *Re* in the vicinity of the impeller can be calculated to be 15971.2 for 150 r·min^{-1}. Then since the speed of each impeller in the group is greater than 150 r·min^{-1}, their *Re* will also be higher than 15971.2. This indicates that the entire flow field is turbulent for all conditions.

$$Re = \frac{\rho N_{\mathrm{rps}} D^2}{\mu} \tag{1}$$

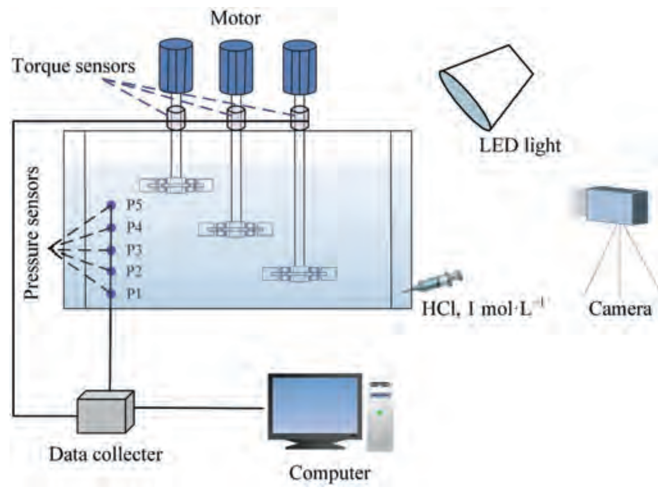

Fig. 3. Experimental setup.

where N_{rps} (r·s^{-1}) is the rotational frequency, D (m) is the impeller diameter, ρ (kg·m^{-3}) is the density of the working medium, and μ (Pa·s) is the dynamic viscosity of the working medium.

2.3.1. Mixing time

Since different injection positions have a large effect on mixing time [41], the injections were standardized at the same bottom position by syringe. The mixing time t_{m} (s) was determined through an acid-base color change experiment. In this work, t_{m} refers to the time from the addition of the HCl solution until the entire tank turns yellow. The specific experimental steps are as follows:

(1) Add 3 ml of 10 g·L^{-1} bromophenol blue solution to the stirred tank and start stirring to ensure it is evenly distributed in the water, at which point the water in the tank turns blue.

(2) To clearly observe the color change caused by acid-base neutralization, add 60 ml of 1 mol·L^{-1} HCl solution first to

Table 1
Specific rotation speed configuration.

Rotation speed combinations	Rotation speed of E1/r·min^{-1}	Rotation speed of E2/r·min^{-1}	Rotation speed of E3/r·min^{-1}	Total power consumption/W	Mixing time/s
M1	200	150	250	1.6061	7.8
M2	200	250	150	2.2983	8.2
M3	150	200	250	1.8452	8.9
M4	150	250	200	2.2681	9.0
M5	200	200	200	1.8265	9.5
M6	250	150	200	1.6304	10.8
M7	250	200	150	1.5873	11.0

bring the pH of the fluid in the tank between 3.0 and 4.6, causing the solution to change from blue to yellow. This was found to be a clearer judge of mixing time in experiments.

(3) Pour 10 ml of 1 mol·L^{-1} NaOH solution into the stirring tank from the top and stir, turning the solution blue again.

(4) Inject 10 ml of 1 mol·L^{-1} HCl solution from position P1 and record the process using a Canon EOS 80D camera until the color of the solution changes uniformly. This time is the mixing time t_m.

2.3.2. Power consumption

The total power consumption P_a (W) is the sum of the power consumption P_w (W) of the three motors, representing the total energy consumed by all the motors during system operation. The calculation equations are as follows:

$$P_w = \frac{2\pi MN}{60} \tag{2}$$

$$P_a = P_{w1} + P_{w2} + P_{w3} \tag{3}$$

where M (N·m) is the average torque during the steady-state stage of the flow field, P_{w1}, P_{w2} and P_{w3} (W) are the power consumption of the top, middle and bottom motors, respectively. N (r·min^{-1}) is the impeller rotation speed.

2.3.3. Mixing energy

The mixing energy in the stirred tank refers to the energy consumed or the energy used to achieve mixing during the process [42]. The total mixing energy W_m of the system can be calculated by the product of the total power P_a and the mixing time t_m by using Eq. (4).

$$W_m = P_a t_m \tag{4}$$

where P_a (W) is the total power consumed by the three impellers, and t_m (s) is the mixing time determined by the acid-base color change experiment.

3. Mathematical Models and Method

3.1. Flow governing equations

The large eddy simulation (LES) model is a numerical simulation method that lies between direct numerical simulation (DNS) and Reynolds-averaged Navier–Stokes (RANS) methods. It offers a good balance between lower computational resource requirements and higher accuracy in simulating flow fields. In LES, the smaller vortices, which are smaller than the filter scale, are filtered out from the turbulence instantaneous motion equations, leaving equations that describe the large eddies. The subgrid-scale stress is introduced into the motion equations of the large eddy flow field to account for the effects of the filtered small eddies on the large eddies. This mathematical model is called the subgrid-scale (SGS) model [43]. For the incompressible flow involved in this work, the continuity equation is as follows:

$$\frac{\partial \bar{\boldsymbol{u}}_i}{\partial \boldsymbol{x}_i} = 0 \tag{5}$$

For an incompressible Newtonian fluid, the Navier–Stokes equations for the instantaneous state, processed through the filtering function, are expressed as:

$$\frac{\partial}{\partial t}(\rho \bar{\boldsymbol{u}}_i) + \frac{\partial}{\partial \boldsymbol{x}_j}\left(\rho \bar{\boldsymbol{u}}_i \bar{\boldsymbol{u}}_j\right) = -\frac{\partial \bar{p}}{\partial \boldsymbol{x}_i} + \frac{\partial}{\partial \boldsymbol{x}_j}\left(\mu \frac{\partial \bar{\boldsymbol{u}}_i}{\partial \boldsymbol{x}_j}\right) - \frac{\partial \boldsymbol{\tau}_{ij}}{\partial \boldsymbol{x}_j} \tag{6}$$

where $\boldsymbol{\tau}_{ij}$ is the subgrid-scale stress tensor, defined as:

$$\boldsymbol{\tau}_{ij} = \bar{\rho}\tilde{\boldsymbol{u}}_i \boldsymbol{u}_j - \bar{\rho}\tilde{\boldsymbol{u}}_i \tilde{\boldsymbol{u}}_j \tag{7}$$

The subgrid-scale turbulence viscosity model is expressed as:

$$\boldsymbol{\tau}_{ij} - \frac{1}{3}\tau_{kk}\boldsymbol{\delta}_{ij} = -2\mu_t \bar{\boldsymbol{S}}_{ij} \tag{8}$$

where δ_{ij} is the Kronecker delta (which is 1 if $i = j$, otherwise 0),τ_{kk} can be added to the filtered pressure or simply neglected in the incompressible flows.

The strain rate tensor for the resolved scales is defined as:

$$\bar{\boldsymbol{S}}_{ij} \equiv \frac{1}{2}\frac{\partial \bar{\boldsymbol{u}}_i}{\partial \boldsymbol{x}_j} + \frac{1}{2}\frac{\partial \bar{\boldsymbol{u}}_j}{\partial \boldsymbol{x}_i} \tag{9}$$

In Ansys Fluent, several subgrid-scale models are provided, such as the Smagorinsky–Lilly model and the wall-adapting local eddy viscosity (WALE) model [44,45]. The WALE model is used in this work because it incorporates a spatial operator, making it more accurate for calculating the near-wall region of wall-bounded flows.

In the WALE model, the eddy viscosity is expressed as:

$$\mu_t = \rho L_S^2 \frac{\left(\boldsymbol{S}_{ij}^d \boldsymbol{S}_{ij}^d\right)^{3/2}}{\left(\bar{\boldsymbol{S}}_{ij}\bar{\boldsymbol{S}}_{ij}\right)^{5/2} + \left(\boldsymbol{S}_{ij}^d \boldsymbol{S}_{ij}^d\right)^{5/4}} \tag{10}$$

$$\boldsymbol{S}_{ij}^d = \frac{1}{2}\bar{g}_{ij}^2 + \frac{1}{2}\bar{g}_{ji}^2 - \frac{1}{3}\boldsymbol{\delta}_{ij}\bar{g}_{kk}^2 \bar{g}_{ij}, \bar{g}_{ij} = \frac{\partial \bar{\boldsymbol{u}}_i}{\partial \boldsymbol{x}_j} \tag{11}$$

L_S refers to the mixing length at the subgrid scale.

$$L_S = \min\left(\kappa d, C_W V^{1/3}\right) \tag{12}$$

where κ is the von Kármán constant. d is the distance to the closest wall, C_W is the nondimensional coefficient called the WALE constant. The WALE constant $C_W = 0.325$, V is the volume of the local grid element.

3.2. Boundary conditions

All numerical simulations in this work were conducted using ANSYS Fluent V19.2, with transient simulations performed on a workstation equipped with an R9 7950X CPU, using a time step of 0.01 s for iterations. The solver settings are as follows:

A three-dimensional model was used, and the effect of gravity was considered. Pressure–velocity coupling was achieved through the SIMPLEC method, with gradient calculations based on the least-squares cell-based discretization method. Pressure, momentum, and other terms were discretized using a second-order upwind scheme. The convergence criterion for all equations was set to a relative residual of less than 10^{-6}. Initial values were generated from steady-state simulation results, followed by transient simulations using the LES model. The subgrid-scale stress model selected was the WALE model, and near-wall treatment was handled using the Werner–Wengle method. The rotation of the impeller zone is managed using the moving reference frame (MRF) model. This approach utilizes a pressure-based solver. The absolute velocity formulation is applied to ensure accurate calculations. Each step is designed to handle the dynamic nature of the rotating zone effectively. The combination of these methods allows for precise modeling of the impeller's rotational effects on the fluid flow within the system.

3.3. Definition of metrics

3.3.1. TKE and turbulent dissipation rate

Since the LES model does not directly compute TKE and its dissipation rate, post-processing is required [46,47]. The turbulent kinetic energy is the sum of grid-resolved TKE (k_{res}) and subgrid-scale TKE (k_{sgs}):

$$k = k_{\mathrm{res}} + k_{\mathrm{sgs}} = \frac{1}{2}\overline{\boldsymbol{u}'\boldsymbol{u}'} + \frac{1}{2}\overline{\boldsymbol{v}'\boldsymbol{v}'} + \frac{1}{2}\overline{\boldsymbol{w}'\boldsymbol{w}'} + \left(\frac{\mu_{\mathrm{sgs}}}{\rho L_S}\right)^2 \tag{13}$$

The total dissipation rate (of the solved and the subgrid scale) can be computed from

$$\varepsilon = \frac{1}{2}\nu\left(\frac{\partial \boldsymbol{u}_i}{\partial \boldsymbol{x}_j} + \frac{\partial \boldsymbol{u}_j}{\partial \boldsymbol{x}_i}\right)^2 + \frac{1}{2}\nu_{\mathrm{sgs}}\left(\frac{\partial \boldsymbol{u}_i}{\partial \boldsymbol{x}_j} + \frac{\partial \boldsymbol{u}_j}{\partial \boldsymbol{x}_i}\right)^2 \tag{14}$$

3.3.2. Fractal dimension

In the mixing process of stirred reactors, turbulence is the most common and complex flow pattern encountered. Its main characteristic is the irregularity of the flow, manifested as irregular fluctuations of flow variables over time and space. Furthermore, turbulence is highly sensitive to initial conditions. Therefore, to enable meaningful comparison and validation, its intrinsic features, such as chaotic characteristics, must be extracted. The highly irregular nature of chaos is also reflected in the infinite complexity of fractals, making fractals an important geometric language for describing chaos.

Fractal dimension is widely used in evaluating the chaotic characteristics of flow fields and model validation. Sarkar and Chaudhuri [48] proposed the differential box counting (DBC) method to calculate the fractal dimension. The fractal dimension F_{d} can be estimated by performing a least-squares fit of $\lg(N_r)$ and $\lg(1/r)$:

$$y = F_{\mathrm{d}}x + c \tag{15}$$

where $y = \lg(N_r)$, $x = \lg(1/r)$, r is the partition ratio, and N_r is the total number of boxes in all grids.

3.3.3. Kolmogorov entropy (K)

In turbulence, the velocity and pressure of the fluid fluctuate dramatically over time and space, exhibiting a high degree of chaos. Kolmogorov entropy is an important indicator used to measure this degree of chaos, it describes the amount of information loss per unit time and is used to quantify chaos and increase in dynamics [49,50]. The increase in dynamics has a profound impact on the flow state [51], and the flow instability in stirred reactors is closely related to the mixing process. Therefore, studying instability is crucial for optimizing mixing performance. The larger the Kolmogorov entropy value, the higher the chaos in the system, and the greater the uncertainty and unpredictability in the flow field. In turbulence, this high degree of chaos is often accompanied by numerous small-scale vortices and complex turbulent structures, indicating the presence of more small-scale vortices in the flow field. Thus, Kolmogorov entropy can assess the level of chaos and turbulence intensity under different flow field configurations. Kolmogorov entropy was calculated by pressure time series in this work. Kolmogorov entropy is defined as follows:

$$K = \lim_{\epsilon \to \infty} \lim_{N \to \infty} \frac{1}{N} \sum_{i=1}^{N} H\left(\epsilon, T^i\right) \tag{16}$$

where ϵ represents the resolution of the system state; $H(\epsilon,T^i)$ denotes the uncertainty of the system state after i transformations. Kolmogorov entropy is calculated by determining the one-dimensional correlation entropy of the time series.

3.4. Hexahedral mesh grid

The mesh used in this work has undergone grid independence verification in earlier work. The F values of the grid used in this work is shown in Fig. S1 [26]. The integral length scale was used to represent all vortices at a given location, and it has been demonstrated that this set of mesh sizes can resolve 80% of TKE.

To ensure computational accuracy while minimizing computational costs, this work uses a structured hexahedral mesh for the refined meshing of the three-shaft stirred reactor. It is worth noting that to improve the solution accuracy near the impeller's rotating domain, the mesh around the impellers and the rotating domain was refined. The structured mesh was constructed using ICEM CFD 19.2, with a minimum mesh size of 5 mm and a total of 110044951 cells. The mesh structure is shown in Fig. 4.

3.5. Model validation

Fractal dimension is a method used to measure the irregularity of complex systems. When combined with chaos theory, it illustrates how certain aspects of a complex system (such as morphology, structure, information, function, time, and energy) locally exhibit similarity to the overall system under specific conditions or processes. In light of this, this work compares the fractal dimensions of wall pressure at different measurement points (locations shown in Fig. 3, including P1 to P5) in both experiments and simulations, aiming to verify the accuracy and reliability of the constructed model. Fig. 5 shows a comparison of the fractal dimensions obtained from experiments and simulations at different axial positions under the M1 (200150250) condition. As seen from the figure, the fractal dimensions extracted from experiments are generally slightly higher than those from the simulations, mainly due to external factors such as mechanical vibrations during the experiments, which increased the complexity of the experimental system. Nevertheless, the average error and maximum error between the experiments and simulations were controlled within 15.60% and 17.59%, respectively, both lower than the 20% threshold, indicating good consistency between the simulation and experimental results.

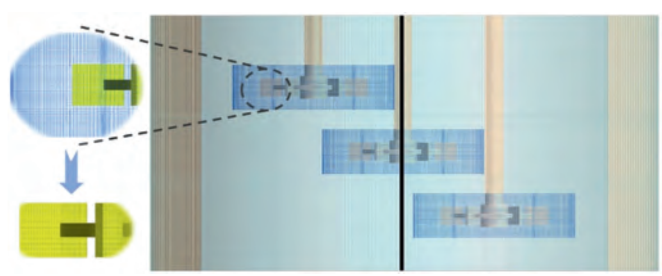

Fig. 4. Hexahedral grid system used in the stirred tank.

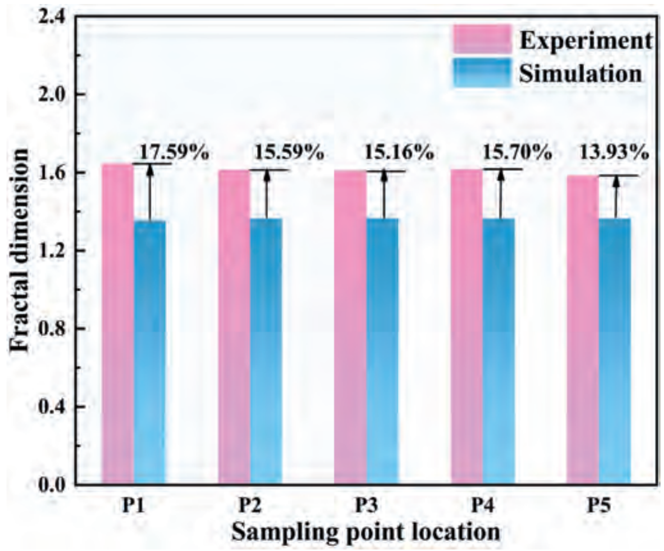

Fig. 5. Fractal dimensions obtained from experiments and simulations at different axial positions.

Fig. 6. Phenomena of decolorization experiments at 5 s: (a) M1; (b) M5; (c) M7.

4. Results and Discussion

4.1. Mixing time

Mixing time is a crucial indicator and direct reflection of mixing performance. Fig. 6 presents the experimental observations at the 5th second under three rotation speed configurations: M1, M5, and M7. In the M1 configuration, only the middle region of the flow field shows a light purple color, while in the M5 configuration, an uncolored area remains on the left side of the flow field. In the M7 configuration, large uncolored areas are observed throughout the entire flow field. It is worth noting that the rotation speed difference result in significant differences in mixing performance.

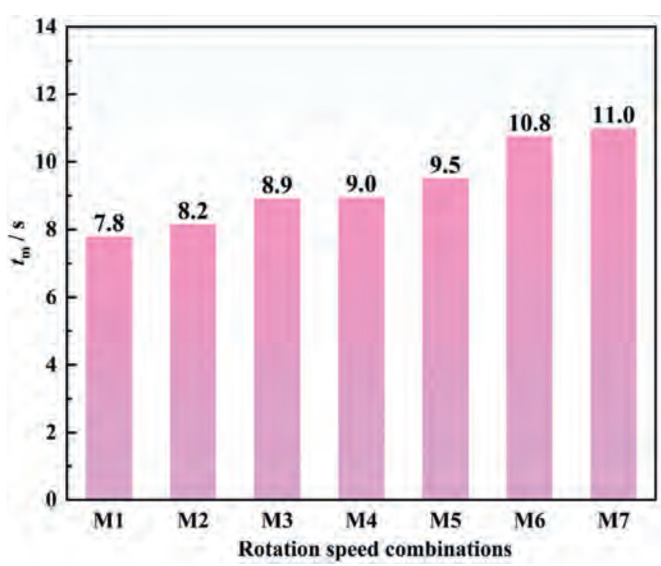

Fig. 7. Mixing times for seven working conditions.

Fig. 7 shows the mixing times for different rotation speed combinations. The mixing time is determined frame by frame through high speed camera capture. It can be observed that M7 has the longest mixing time, while M1 has the shortest, with a difference of 3.2 s (29.09%). Using the no-speed-difference group M5 as a reference, the changes in mixing time for the groups with speed differences range from −1.5 s to 1.7 s (15.46% to 18.07%). This indicates that rotation speed difference has a significant impact on mixing performance, highlighting the varying influence of each impeller on mixing performance. This variability is worth further investigation.

Compared to the M5 condition, the mixing performance of M7 decreased, while that of M1 improved. This phenomenon suggests that increasing the rotation speed of E1 has a smaller effect on mixing, whereas E2 and E3 have a greater impact. Notably, when keeping the rotation speed of E1 constant, the mixing times follow the pattern: M1 < M2, M3 < M4, and M6 < M7. This indicates that increasing the rotation speed of E3 results in a reduction in mixing time, demonstrating that E3 has a greater influence on mixing performance compared to E2. When the combined speed of E2 and E3 reaches its maximum (M3 and M4), the mixing time is longer than in M1 and M2, indicating that the reduction in E1's rotation speed leads to a relative decline in mixing performance. The mixing time results show that the E3 impeller has the greatest influence on mixing performance and is most sensitive to speed changes. However, when E1's rotation speed drops to around 200 $r\cdot min^{-1}$, it leads to a decrease in mixing performance. Overall, a reasonable distribution of rotation speed is crucial for enhancing mixing performance. However, in stirred reactors, power consumption is also an important factor that cannot be ignored.

4.2. Power consumption and mixing energy

As mentioned above, the torque data were taken from the torque sensors of the motors in the experiments and the average of collected data was taken. The sensors were zeroed before each acquisition. The average torque values of the three impellers for each condition shown in Table 2. To further compare the power consumption of each shaft under different rotation speed configurations, we plotted Fig. 8(a). It can be observed that the power consumption follows the order: M2 > M4 > M3 > M5 > M6 > M7 > M1. Notably, the total power consumption of M1 is approximately 0.2204 W (12.07%) lower than that of M5. Additionally, in most conditions, E2 accounts for the largest share of power consumption, followed by E3. This is because the impellers of E2 and E3 disturb more fluid and generate higher torque, while the upper impeller E1, being closer to the liquid surface, is less affected by fluid pressure, resulting in relatively lower torque. The power consumption analysis indicates that at high

Table 2
Value of average torques for different rotation speed combinations.

Rotation speed combination	M_a of E1/N·m	M_a of E2/N·m	M_a of E3/N·m
M1	0.0169	0.0310	0.0293
M2	0.0173	0.0633	0.0179
M3	0.0095	0.0459	0.0281
M4	0.0103	0.0638	0.0209
M5	0.0195	0.0465	0.0212
M6	0.0278	0.0301	0.0205
M7	0.0160	0.0422	0.0182

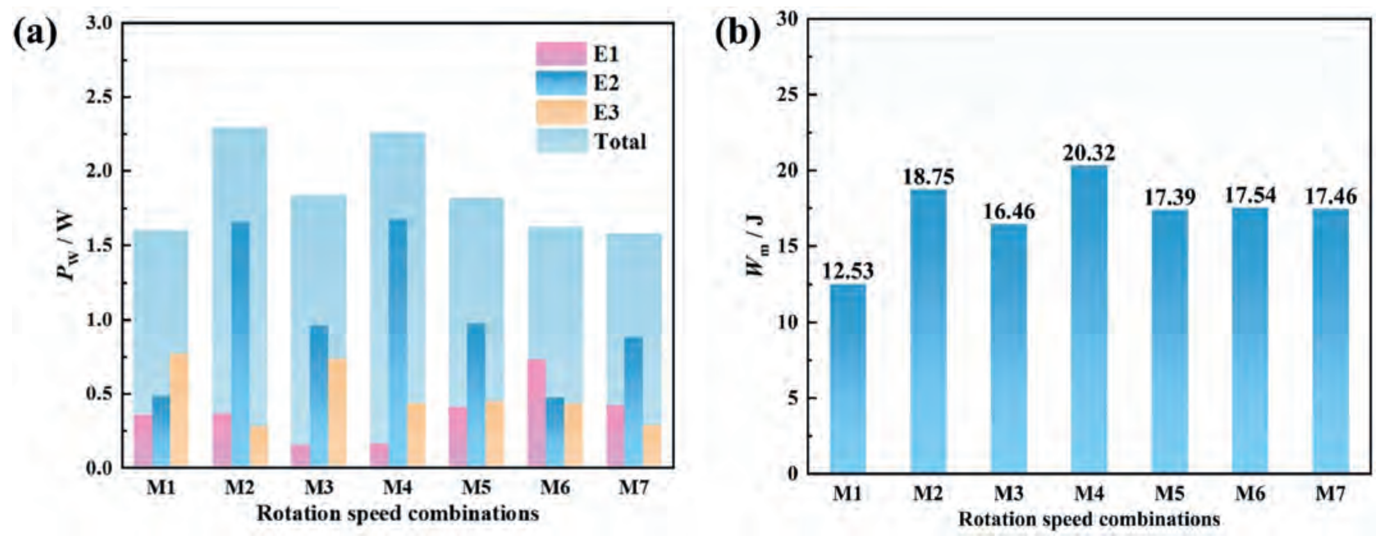

Fig. 8. Power consumption and mixing energy: (a) power consumption of E1, E2 and E3 and total; (b) mixing energy.

rotation speed, E2 leads to a rapid increase in power consumption, which is also a key reason why M1, with a lower rotation speed of E2, is the most energy-efficient condition. Therefore, when considering energy savings, it is advisable to minimize the rotation speed of E2.

In practical production processes, designing stirred reactors typically requires a comprehensive consideration of both mixing performance and power consumption. To this end, we introduced the concept of mixing energy to evaluate the overall performance of both aspects. Mixing energy refers to the amount of energy input into the system during stirring to achieve uniform mixing of different components. Generally, the greater the mixing energy, the more energy is required to complete the mixing process, leading to poorer overall performance. Fig. 8(b) presents the mixing energy for different operating conditions. Compared to M5, only M1 and M3 (150200250) show reductions in mixing energy, by approximately 4.8065 J (27.95%) and 0.9291 J (5.34%), respectively. Therefore, M1 demonstrates the best overall performance in terms of both mixing performance and power consumption. This result strongly supports the notion that a reasonable rotation speed distribution strategy can enhance mixing performance while effectively reducing energy consumption, thereby fully exploiting the potential mixing capacity of multi-shaft stirred reactors. To maximize the use of rotation speed difference to unlock the mixing potential of three-shaft stirred reactors and to identify the most optimal speed distribution scheme, it is essential to conduct in-depth studies on the underlying mechanisms. This may be related to the redistribution of energy in the flow field, which requires further investigation through chaos analysis and flow field simulations to explore the deeper causes.

4.3. Characterization of chaos

In turbulence, the Kolmogorov entropy of pressure fluctuations quantifies the degree of chaos in a dynamic system. We studied the magnitude and distribution of Kolmogorov entropy under various conditions. Fig. 9 shows the Kolmogorov entropy values (*K* value)

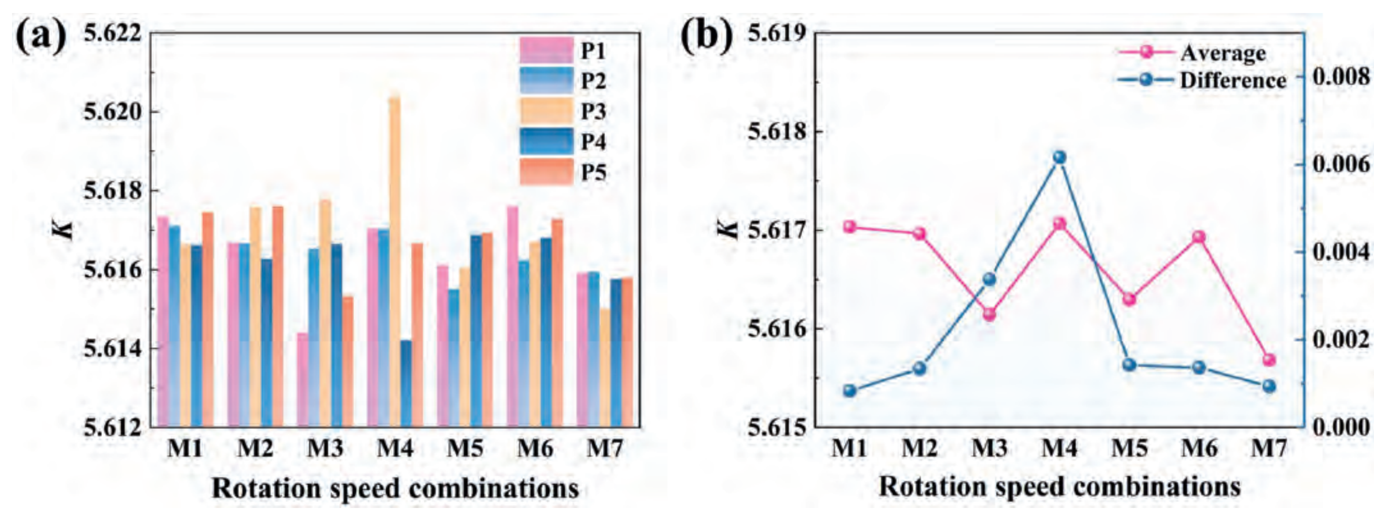

Fig. 9. *K*-entropy based on wall pressure at 5 positions in the axial direction: (a) *K* entropy values for five sampling positions; (b) mean values and maximum difference for different sampling locations.

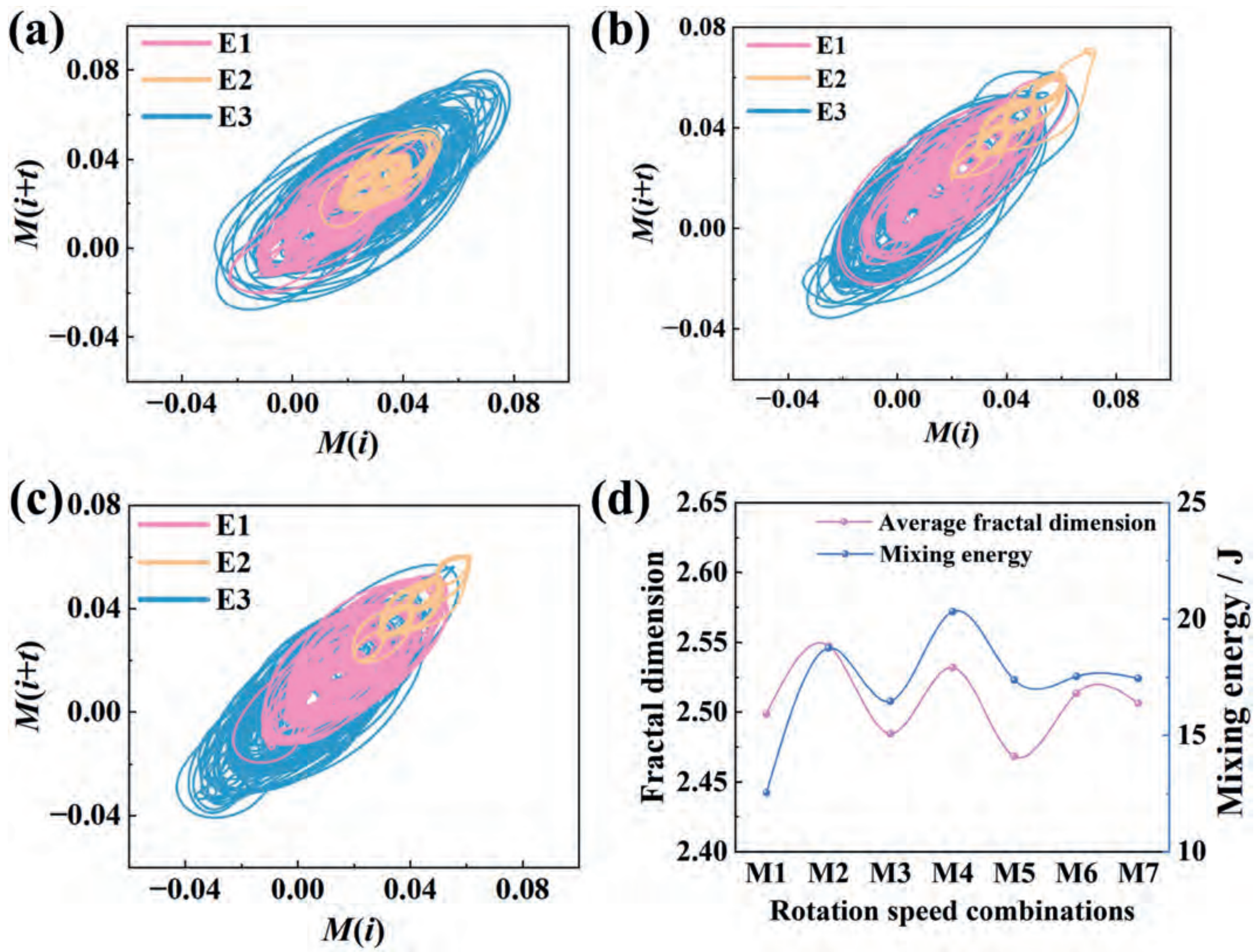

Fig. 10. Torsional attractor and average fractal dimension and mixing energy: (a) M1; (b) M5; (c) M7; and (d) average fractal dimension and mixing energy for seven working conditions.

at points P1 to P5 under different conditions. In Fig. 9(b), it can be observed that the average K value is highest under condition M1 and lowest under M7. This indicates that the system demonstrates greater chaos and dynamic complexity under the M1 condition. A higher K value also suggests that the M1 configuration generates more small-scale vortex structures in the flow field, which effectively disrupt the self-organized structure caused by large-scale vortex structures. This enhances the energy cascade effect, promoting efficient energy and mass transfer throughout the system, directly reflected in M1 having the shortest mixing time among the seven conditions. Similarly, the increase in mixing time under the M7 condition can be attributed to its lowest average K value. Additionally, the smallest differences in Kolmogorov entropy across different locations in the M1 condition reflect a relatively uniform degree of chaos in various regions, indicating a more homogeneous flow field, further reinforcing the even energy distribution. It is noteworthy that although M7 also has small Kolmogorov entropy differences, its overall mixing performance is the worst. This is because M7 has the lowest average K value, showing that the overall mixing performance is not only related to the instability differences across regions but also closely tied to the overall magnitude of instability. Therefore, a reasonable rotation speed difference configuration can increase dynamics and reduce difference between regions, improving overall mixing performance.

The biggest challenge in the intelligentization of stirred reactors is that conventional methods for evaluating mixing performance cannot provide real-time and effective feedback. However, using chaotic characteristics to represent mixing performance is clearly an effective approach, as demonstrated by Kolmogorov entropy, which can effectively characterize or explain changes in mixing performance. The downside is that obtaining K requires the analysis of additional signals, specifically pressure fluctuation data, which are not commonly collected during the industrial operation of stirred reactors. This inevitably increases the complexity and installation cost of industrial equipment. In our previous work, we proposed a strategy to represent mixing performance using the average fractal dimension of torque attractors. In this work, we attempt to further analyze the internal mechanisms of multi-shaft stirred reactors driven by rotation speed difference using this method. In multi-shaft, multi-impeller stirring systems, torque signal fluctuations reflect the interactions between the impellers and the fluid, as well as between the impellers themselves through the flow field. Investigating the dynamic changes in torque signals under different rotation speed combinations helps in understanding the variations in flow states.

To study this complex dynamic behavior, we introduced the chaotic attractor of torque for analysis to observe the degree of chaos in the flow field, providing theoretical support for reducing impeller energy consumption, optimizing the mixing process, and improving overall mixing performance. Similarly, the chaotic attractor of torque is derived from the time series of the torque signal and the phase space reconstruction is used, the original waveform of which is shown in Fig. S2. As shown in Figs. 10 and S3, the attractor shape reveals that, under the M1 condition, the torque attractors for different shafts are more tightly clustered and nested in phase space, whereas those in M5 and M7 are more scattered and disordered, with a tendency to separate. This weaker interaction between the impellers and the resulting lower energy transfer lead to weaker mass transfer compared to M1, which accounts for the differences in mixing performance. The reason behind this lies in how the rotation speed difference intensify the variation in interactions between the impellers and the fluid, causing changes in the flow field structure, which needs to be verified in the next section with flow field simulation results. Additionally, our work further validates the broad applicability of the characterization strategy we previously proposed [27].

4.4. Numerical simulation and discussion

To analyze the internal mechanisms from the perspectives of flow field structure and evolution, and to further optimize mixing performance, we conducted an in-depth analysis of three different conditions: M1, which exhibited the best mixing performance, M7, which had the worst mixing performance, and M5, with no rotation speed difference as a control. The goal is to gain a deeper understanding of the underlying causes and mechanisms.

4.4.1. Velocity flow field analysis

Fig. 11(a), (b), and (c) show the iso-surface plots of areas where the velocity is greater than 0.2 $m\cdot s^{-1}$ within the three-shaft stirred reactor, along with velocity contour plots at the *XY* cross-section of

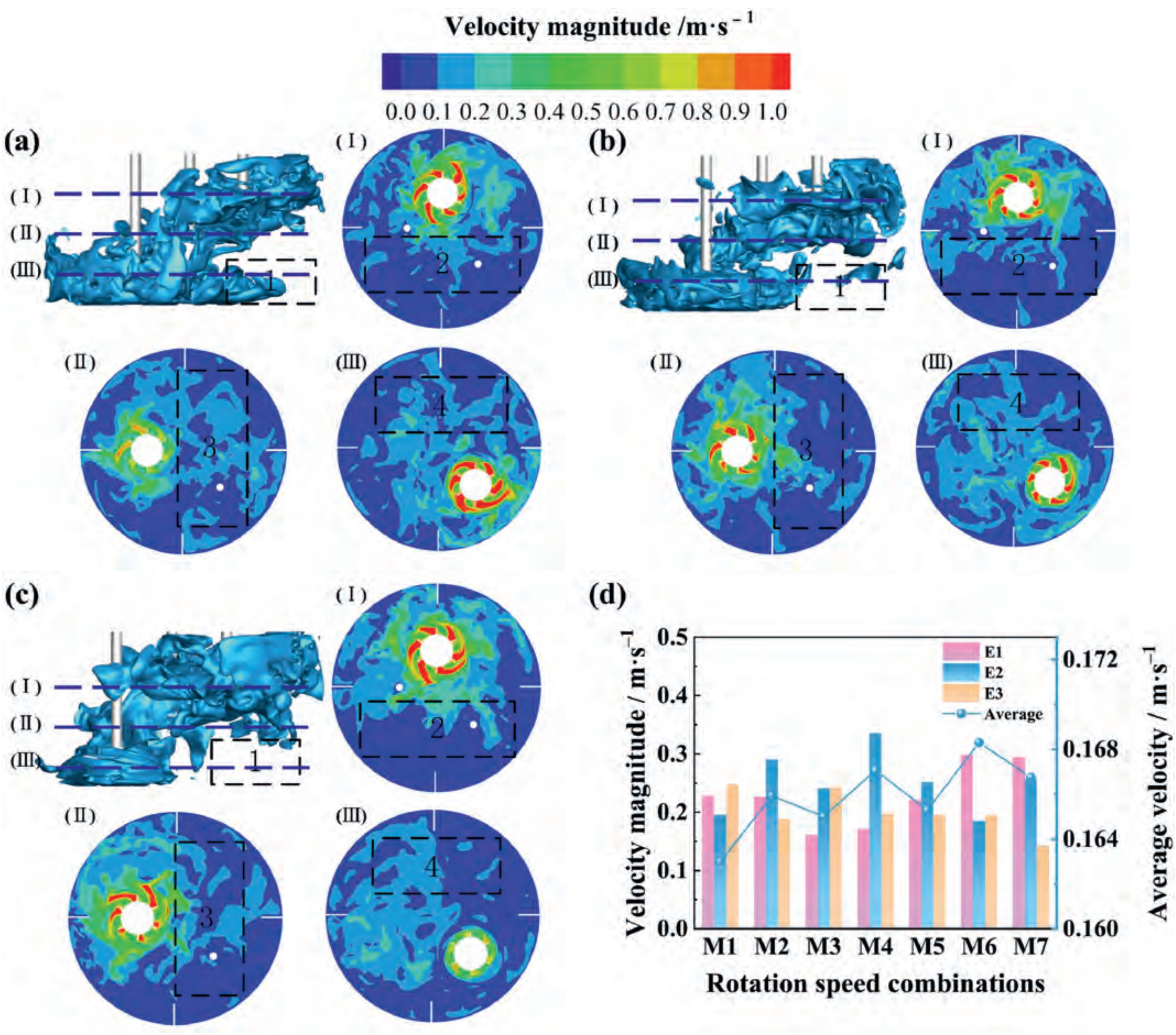

Fig. 11. Velocity contours and iso-surfaces for different rotation speed combinations: (a) M1; (b) M5; (c) M7; and (d) The velocity statistics on the impeller plane and the overall average velocity (the dotted lines in the figure show the locations of the three cross sections).

the three impellers. It can be observed that high-velocity regions are mainly concentrated around the E2 impeller, while areas farther from E1 and E3 have relatively lower velocity distributions. Compared to M5, M1 and M2 (Fig. S4) exhibit higher uniformity in velocity distribution within region 1. In contrast, the improvement in M3 and M4 is relatively limited, and M6 and M7 even show deterioration. Further comparative analysis of regions 2, 3, and 4 reveals that M1's flow field not only has a more uniform velocity distribution but also shows a significant overall speed increase. In M3 and M4 (Figs. S5 and S6), the reduction in the rotation speed of the upper impeller E1 results in a smaller high-velocity area in the upper region, limiting further improvement in mixing performance. Although M6 and M7 increased the rotation speed of the upper impeller E1, the overall uniformity of the velocity distribution in the flow field did not improve significantly (Figs. S7 and 11 (c)) due to the reduction in E3's rotation speed. These results collectively indicate that M1 exhibits the best velocity distribution uniformity among all the groups and also reveal that E1's contribution to overall mixing has reached saturation at a speed of 200 $r \cdot min^{-1}$. Meanwhile, the middle impeller E2 did not significantly increase the distribution of the high-velocity fluid region around it. However, E2 consistently maintains the maximum coverage of the high-velocity region around it, which is due to its position as a bridge with stronger interactions with E1 and E3, and also suggests that it may have reached the critical value of the flow field conditioning capability at 150 $r \cdot min^{-1}$. This saturation characteristic allowed the overall mixing performance of the system to change little as the speed was adjusted. And increasing the rotation speed of the E3 impeller significantly optimizes the uniformity of the overall flow field velocity distribution.

From a quantitative perspective, Fig. 11(d) provides key data points, the average values of the velocities at all points in the three cross-sections of the simulated data were extracted separately, and the average of the mean velocities of the three cross-sections were calculated as fold plot. It specifically showing the average velocity in the *XY* plane of each impeller as well as the average velocity of the entire flow field. Although M1's overall average velocity is lower than that of the other groups, its velocity distribution across the three planes is relatively balanced. In contrast, while M6 and M7 exhibit the highest overall average velocities, their velocity distributions across the three planes show significant disparities. This indicates that excessive velocity leads to more kinetic energy being dominated by large-scale vortices, suppressing the generation and evolution of small-scale vortices, ultimately reducing turbulence mixing efficiency. This finding further confirms that the rotation speed configuration of M1 effectively promotes the generation of small-scale vortices, thereby enhancing mixing performance.

In summary, increasing the rotation speed of the E3 impeller is an effective approach to improving the uniformity of velocity distribution in the flow field and enhancing overall mixing performance. Specifically, maintaining E1 at an appropriate speed, moderately reducing the rotation speed of E2, and increasing the rotation speed of E3 can significantly strengthen the weak mixing regions in the flow field, maximizing the uniformity of the velocity distribution and further optimizing the mixing process. To further investigate the energy cascade efficiency between small-scale and large-scale vortices and to visually analyze energy transfer and distribution, a more detailed analysis of the turbulent kinetic energy distribution is required.

4.4.2. TKE and dissipation rate statistics and analysis

Fig. 12 shows the TKE distribution contour maps at the *XY* cross-sections of the three impellers, where the maximum difference is obtained by subtracting the minimum value from the maximum value in the statistically averaged velocities of the three cross sections. In Fig. 12(b), (c) and (d), it is clear that M1 exhibits significantly higher overall TKE compared to M5 and M7, particularly in regions 1, 2, and 3, where this difference is especially pronounced. This phenomenon demonstrates that a well-configured rotation speed difference can significantly enhance the degree of turbulence in the flow field, thereby optimizing the mixing performance of the system. However, the specific impact of each impeller on the turbulence level requires further investigation.

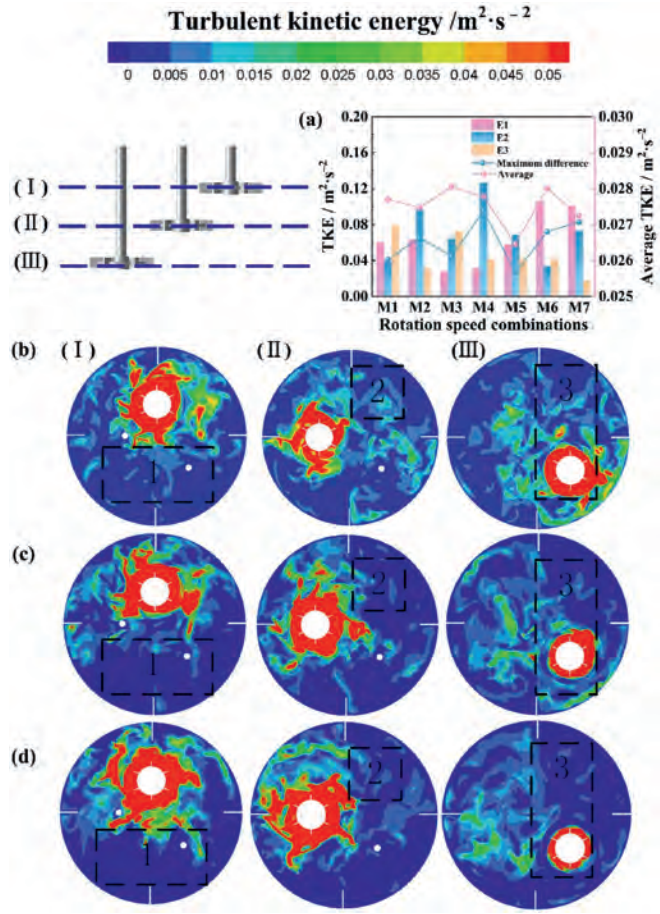

Fig. 12. TKE contours for different rotation speed combinations: (a) The TKE statistics on the impeller plane and the overall average TKE; (b) M1; (c) M5; and (d) M7.

During the work, we found that although M7 increased the rotation speed of impeller E1, it only enhanced the turbulent kinetic energy in the vicinity of the impeller without improving the energy distribution in the whole plane. However, its reduction of the rotation speed of E3 significantly deteriorates the uniformity of the TKE distribution in the E3 plane, which ultimately leads to a reduction in the mixing performance. Conversely, while M1 reduced the speed of the E2 impeller, the energy distribution in region 2 on the E2 plane became more uniform (as shown in Fig. 12 (a)). This improvement was primarily due to the increased rotation speed of E3, which strengthened the interaction between E3 and E2, facilitating energy transfer in these regions. The analysis above shows that M1 achieves excellent TKE distribution across all three planes, indicating that the M1 configuration allows fluid from different regions to actively participate in energy transfer, effectively redistributing energy in the flow field. This further confirms that increasing E3's rotation speed not only enhances energy transfer in the E3 region but also, through interaction with E2, further promotes energy transfer in the E2 region, ultimately improving energy transfer efficiency throughout the flow field. Further analysis of the dissipation rate reveals that while M1's reduction of E2's speed slightly decreased the dissipation rate near the impeller, this adjustment significantly improved the dissipation rate distribution in areas farther from the impellers (Fig. S12 (b), (c), and (d)). This enhancement in the overall uniformity of the dissipation rate distribution improved mixing performance, further confirming the importance of increasing E3's rotation speed for enhancing energy transfer across the entire flow field.

From a quantitative perspective, Fig. 12(d) provides key data points, displaying the average TKE on the *XY* plane of each impeller, along with the overall flow field's average TKE and maximum difference between three planes. Among the six configurations with rotation speed differentials, the TKE in M7 is the lowest, yet it has the largest TKE variation across the three planes. This indicates that, while M7 increases average TKE, it greatly intensifies axial TKE distribution unevenness, leading to reduced mixing performance. Although M3, M4, and M6 have slightly higher average TKE than M1, M1 shows the smallest TKE difference, with a more uniform distribution. This demonstrates that M1 achieves improved mixing performance by enhancing overall energy distribution. Similarly, statistical analysis of dissipation rate also indicates that M1 exhibits the most uniform dissipation rate distribution (Fig. S12(a)), reflecting a more balanced energy transfer across the flow field.

In conclusion, M1 improves the overall mixing performance because it exhibits an overall high and most uniform distribution of turbulent kinetic energy and dissipation rate in both radial and axial directions, indicating that the turbulence intensity is relatively equalized in different regions. From an energy transfer perspective, setting E1 to an optimal rotation speed, minimizing E2, and maximizing E3 greatly enhances energy transfer, boosting mixing performance. This result aligns with the velocity analysis, confirming the effectiveness and superiority of this rotation speed configuration strategy.

4.5. Mechanism analysis

As described, through experiments, we found that rotation speed difference can significantly improve the mixing performance and optimize the energy distribution in the flow field. This work further shows that merely enhancing the mixing efficiency of a single impeller or a local region is far from being sufficient to achieve the optimization of the overall performance, but may instead lead to an excessive concentration of local energy, which in turn triggers uneven flow and hinders the transfer of matter and energy. Therefore, improving the overall mixing performance should be taken as the goal, specifically, through the differential configuration of the rotational speed of each impeller, reducing the phase difference between the regions, and opening up the transmission channel of matter and energy, so as to improve the overall mixing performance. A key mechanism in stirred reactors where bidirectional energy and momentum transfer between waves and vortices optimizes momentum propagation and homogenizes fluid distribution. As shown in Fig. 13, when the rotation speed of each impeller is consistent, the flow field tends to be stable, and the mass and energy transfer efficiency is low; while when there is a difference in the rotation speed, the increase in dynamics of the flow field is significantly enhanced, resulting in turbulence that is more likely to occur and accelerating the transformation of the solitary wave to the diffuse wave [18,52]. This process prompts the

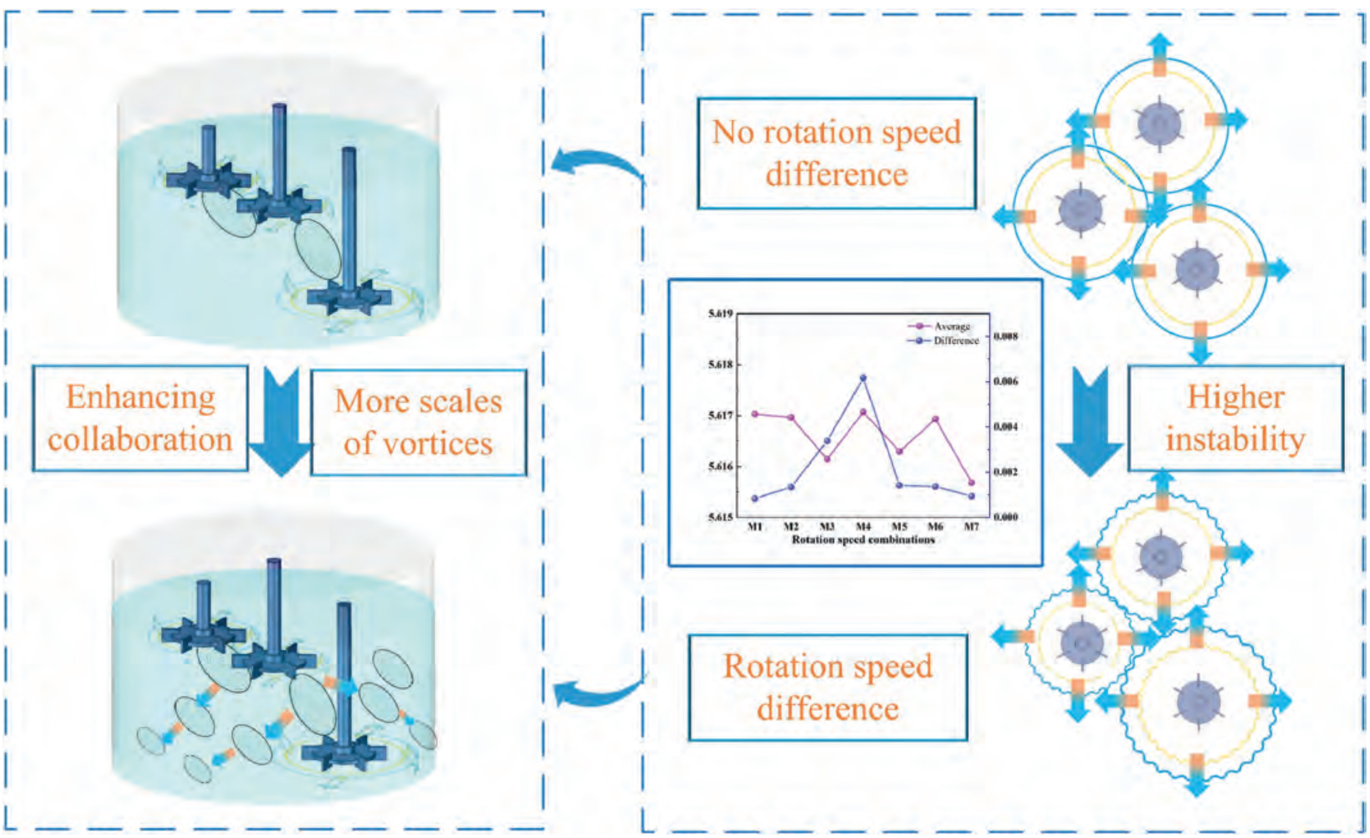

Fig. 13. Schematic diagram of rotation speed difference to enhance instability. The line graphs (Fig. 9(b)) present the mean and maximum differences across the sampling locations.

flow field to rapidly generate multi-scale vortex structures, thus stimulating the energy cascade effect and transferring energy from large scale to small scale, forming a complete wave–vortex coupling process. As a result, the strong instability brought about by the difference in the rotation speed makes the wave propagation paths more complex and diversified, the interactions between vortices more intense and random, and the transport channels of matter and energy more efficient, which is ultimately reflected in the significant enhancement of the mixing performance.

5. Conclusions

This work combines experiments and CFD simulations to compare and analyze the mixing performance and chaotic characteristics of a three-shaft, three-impeller stirred reactor under different rotation speed combinations. It emphasizes the advantages of rotation speed difference in enhancing overall instability and redistributing energy in the flow field. The main conclusions are as follows:

(1) The experiments compared mixing time, power consumption, and mixing energy under different configurations, revealing that a proper rotation speed difference configuration can effectively achieve energy savings and efficient operation. M1 (200150250) performed best, reducing mixing time, power consumption, and mixing energy by 1.7 s (17.89%), 0.2204 W (12.07%), and 4.8065 J (27.95%), respectively, compared to M5 (200200200). Results indicate that the E3 impeller has the most significant impact on the flow field.

(2) Kolmogorov entropy analysis shows that while enhancing flow field instability positively impacts the mixing process, excessive differences in Kolmogorov entropy between different locations can cause uneven flow distribution, hindering mass transfer efficiency. The M1 configuration improved the proportion of small-scale vortex structures by uniformly increasing degree of chaos, thus enhancing mixing performance.

(3) Flow velocity analysis visually depicted the direct influence of each impeller on the mixing process. Specifically, E1's contribution to mixing saturates at 200 $r \cdot min^{-1}$, while increasing E3's rotation speed optimizes weak mixing areas and significantly improves velocity distribution uniformity, strengthening the mixing process. This finding explains M1's superior performance.

(4) Further analysis of energy distribution in the flow field shows that rotation speed difference significantly increase overall TKE and dissipation rate. M1 exhibited the most uniform distribution, indicating balanced turbulence intensity across regions and an enhanced energy cascade effect, boosting mass transfer efficiency. Increasing E3's rotation speed not only promotes energy transfer in the E3 region but also strengthens interactions with E2 and E1, improving overall energy transfer and optimizing the mixing process. Overall, maintaining E1 at an appropriate rotation speed, E2 at the lowest, and E3 at the highest enhances energy transfer and the energy cascade process, ultimately improving mixing efficiency.

In summary, rotation speed difference enhance impeller interactions by adjusting rotation speed distribution, intensifying flow field instability, and strengthening the energy cascade effect between large-scale and small-scale vortices. Localized instability improvements do not necessarily improve overall mixing and may concentrate energy in certain areas, leaving others with low mixing efficiency, causing uneven flow and poor mass transfer. Therefore, instability improvement must be comprehensive and uniform. This work, based on fluid dynamics and turbulence theory, demonstrates that a reasonable rotation speed configuration effectively achieves energy savings and efficiency. Furthermore, the development of intelligent stirred reactors should focus on assigning distinct roles to each impeller and tailoring the operating conditions of each impeller to its specific function, allowing for differentiated and personalized control. Therefore, this work provides a theoretical basis for the development of intelligent stirring technology in the future and also provides new ideas for the sustainable development of stirred reactors in the field of large-scale chemical industry.

CRediT Authorship Contribution Statement

Shuang Qin: Writing – original draft, Methodology, Data curation. Tong Meng: Writing – original draft, Data curation. Yu Wang: Validation, Software. Yundong Wang: Project administration. Changyuan Tao: Funding acquisition. Qian Zhang: Writing – review & editing. Bing Li: Funding acquisition. Zuohua Liu: Supervision, Conceptualization.

Data Availability

The original data that support the findings of this work are available on request from the corresponding author.

Declaration of Competing Interest

The authors declare that they have no known competing financial interests or personal relationships that could have appeared to influence the work reported in this paper.

Acknowledgements

This work was supported by the National Natural Science Foundation of China (22078030, 52021004), National Key Research and Development Project (2019YFC1905802), Key Project of Independent Research Project of State Key Laboratory of Coal Mine Disaster Dynamics and Control (2011DA105287-zd201902), Chongqing Natural Science Foundation Innovation and Development Joint Fund Project (CSTB2022NSCQ-LZX0014), Hubei Three Gorges Laboratory Open/Innovation Fund (SK211009, SK215001), and Fundamental Research Funds for Central Universities (2022CDJQY-005). At the same time, this work also received funding from the China Scholarship Council.

Supplementary Material

Supplementary data to this article can be found online at https://doi.org/10.1016/j.cjche.2025.04.024.

References

[1] S.A.F. Leite, B.S. Leite, D.J.O. Ferreira, B.E.L. Baêta, J.V.H. Dangelo, The effects of agitation in anaerobic biodigesters operating with substrates from swine manure and rice husk, *Chem. Eng. J.* 451 (2023) 138533.

[2] J.Y. Dong, Y.L. Wu, X.C. Liu, C.K. Zhang, S.M. Wang, J. Wen, CFD-PBE simulation of *para*-xylene crystallization behavior and process amplification under different operating conditions, *Ind. Eng. Chem. Res.* 62 (36) (2023) 14657–14670.

[3] Y.R. Wang, Q. Yang, Y.N. Du, H.Q. Chen, Evaluation of the impact of stirring on the formation, structural changes and rheological properties of ovalbumin fibrils, *Food Hydrocoll.* 128 (2022) 107615.

[4] F. Scargiali, A. Brucato, G. Micale, A. Tamburini, On the reduction of power consumption in vortexing unbaffled bioslurry reactors, *Ind. Eng. Chem. Res.* 59 (16) (2020) 8037–8045.

[5] G.Y. Shang, K. Cui, W.F. Cai, X.N. Hu, P.K. Jin, K. Guo, A 20 L electrochemical continuous stirred-tank reactor for high rate microbial electrosynthesis of methane from CO_2, *Chem. Eng. J.* 451 (2023) 138898.
[6] G.D. Zhang, X.Y. Shi, F. Wang, Methane hydrate production using a novel spiral-agitated reactor: promotion of hydrate formation kinetics, *AIChE J.* 68 (1) (2022) e17423.
[7] E. Villermaux, Mixing versus stirring, *Annu. Rev. Fluid Mech.* 51 (2019) 245–273.
[8] P.E. Dimotakis, Turbulent mixing, *Annu. Rev. Fluid Mech.* 37 (2005) 329–356.
[9] L. Torrente-Murciano, J.B. Dunn, P.D. Christofides, J.D. Keasling, S.C. Glotzer, S. Y. Lee, K.M. Van Geem, J. Tom, G.H. He, The forefront of chemical engineering research, *Nat. Chem. Eng.* 1 (1) (2024) 18–27.
[10] E.K. Nauha, O. Visuri, R. Vermasvuori, V. Alopaeus, A new simple approach for the scale-up of aerated stirred tanks, *Chem. Eng. Res. Des.* 95 (2015) 150–161.
[11] P. Vrábel, R.G.J.M. van der Lans, K.C.A.M. Luyben, L. Boon, A.W. Nienow, Mixing in large-scale vessels stirred with multiple radial or radial and axial up-pumping impellers: modelling and measurements, *Chem. Eng. Sci.* 55 (23) (2000) 5881–5896.
[12] M.T. Castro, J.D. Ocon, Novel designs of blade mixer impellers from the discrete element method and topology optimization, *Chem. Eng. J.* 490 (2024) 151863.
[13] T.A. Wyrobnik, S. Oh, A. Ducci, M. Micheletti, Engineering characterization of the novel bach impeller for bioprocessing applications requiring low power inputs, *Chem. Eng. Sci.* 252 (2022) 117263.
[14] B. Delacroix, L. Fradette, F. Bertrand, B. Blais, Which impeller should be chosen for efficient solid–liquid mixing in the laminar and transitional regime? *AIChE J.* 67 (11) (2021) e17360.
[15] C. Sirasitthichoke, S. Salloum, P.M. Armenante, Power number and hydrodynamic characterization of a stirred vessel equipped with a retreat-blade impeller and different types of pharmaceutical single baffles, *Chem. Eng. Sci.* 257 (2022) 117725.
[16] T. Wang, H. Yu, R. Xiang, X.M. Chen, X. Zhang, Performance and unsteady flow characteristic of forward-curved impeller with different blade inlet swept angles in a pump as turbine, *Energy* 282 (2023) 128890.
[17] J. Stelmach, C. Kuncewicz, T. Jirout, F. Rieger, Mixing tank hydrodynamics and mixing efficiency for propeller impellers, *Chem. Eng. Res. Des.* 199 (2023) 460–472.
[18] X. Xiong, S.S. Wang, P.Q. Liu, C.Y. Tao, Y.D. Wang, Z.H. Liu, Numerical investigation on intensified mixing performance with modified dual impeller, *Chem. Eng. Sci.* 274 (2023) 118698.
[19] X.Y. Tang, F.C. Qiu, P.Q. Liu, H. Li, Z.H. Liu, Revealing chaotic advection dynamics in the chaotic mixing of non-Newtonian fluids within a stirred tank employing a twisted-punched impeller, *Ind. Eng. Chem. Res.* 63 (32) (2024) 14259–14274.
[20] J. Aubin, C. Xuereb, Design of multiple impeller stirred tanks for the mixing of highly viscous fluids using CFD, *Chem. Eng. Sci.* 61 (9) (2006) 2913–2920.
[21] M. Wu, N. Jurtz, L. Hohl, M. Kraume, Multi-objective geometrical optimization of single and dual impeller stirred tanks: an application of the mean age theory approach, *Chem. Eng. Res. Des.* 203 (2024) 709–720.
[22] J.C. Long, X.B. Zhan, F. Guo, Z.B. Sun, B.J. Shen, Y. He, X.W. Li, Study of hydrodynamics and flow characteristics in a twin-blade planetary mixer with non-Newtonian fluids, *AIChE J.* 68 (10) (2022) e17797.
[23] G. Ascanio, M. Brito-Bazán, E.B. La Fuente, P.J. Carreau, P.A. Tanguy, Unconventional configuration studies to improve mixing times in stirred tanks, *Can. J. Chem. Eng.* 80 (4) (2002) 558–565.
[24] G. Ascanio, S. Foucault, M. Heniche, C. Rivera, P.A. Tanguy, Chaotic mixing in stirred vessels: a new strategy to enhance homogeneity, *Ing. Mec. Tecnol. Desarro.* 1 (2005) 209–214.
[25] H. Ameur, 3D hydrodynamics involving multiple eccentric impellers in unbaffled cylindrical tank, *Chin. J. Chem. Eng.* 24 (5) (2016) 572–580.
[26] T. Meng, Y. Wang, S.S. Wang, S. Qin, Q. Zhang, Y.D. Wang, C.Y. Tao, Y.Q. Xu, Z. H. Liu, Exploration of multishafts stirred reactors: an investigation on experiments and large eddy simulations for turbulent chaos and mixing characteristics, *Ind. Eng. Chem. Res.* 63 (5) (2024) 2441–2456.
[27] T. Meng, J. Yang, S.S. Wang, Y. Wang, S. Qin, Y.D. Wang, C.Y. Tao, Q. Zhang, Z. H. Liu, Multi-shaft stirred reactors mixing efficiency: rapid characterization strategy based on chaotic attractors, *AIChE J.* 70 (10) (2024) e18510.
[28] H.S. Dou, Origin of Turbulence: Energy Gradient Theory, Springer, Singapore, 2022.
[29] P.A. Tanguy, G. Ascanio, Mixing of shear-thinning fluids with dual off-centred impellers, *Can. J. Chem. Eng.* 83 (3) (2005) 393–400.
[30] H. Yao, J.J. Tang, Z.H. Liu, C.Y. Tao, Y.D. Wang, Chaotic mixing intensification and flow field evolution mechanism in a stirred reactor using a dual-shaft eccentric impeller, *Ind. Eng. Chem. Res.* 61 (26) (2022) 9498–9513.
[31] S.S. Wang, H. Li, C.Y. Tao, R.L. Liu, Y.D. Wang, Z.H. Liu, Study on cavern evolution and performance of three mixers in agitation of yield-pseudoplastic fluids, *Chin. J. Chem. Eng.* 55 (2023) 111–122.
[32] J. Aubin, D.F. Fletcher, C. Xuereb, Modeling turbulent flow in stirred tanks with CFD: the influence of the modeling approach, turbulence model and numerical scheme, *Exp. Therm. Fluid Sci.* 28 (5) (2004) 431–445.
[33] J.B. Joshi, N.K. Nere, C.V. Rane, B.N. Murthy, C.S. Mathpati, A.W. Patwardhan, V.V. Ranade, CFD simulation of stirred tanks: Comparison of turbulence models (Part II: axial flow impellers, multiple impellers and multiphase dispersions), *Can. J. Chem. Eng.* 89 (4) (2011) 754–816.
[34] J.B. Joshi, N.K. Nere, C.V. Rane, B.N. Murthy, C.S. Mathpati, A.W. Patwardhan, V.V. Ranade, CFD simulation of stirred tanks: Comparison of turbulence models. Part I: radial flow impellers, *Can. J. Chem. Eng.* 89 (1) (2011) 23–82.
[35] Z.T. Jia, S.F. Zhang, K.F. Fang, B. Kong, M.H. Xie, Q.H. Zhang, C. Yang, Assessment of stress-blended eddy simulation on prediction of flow characteristics in a Rushton impeller stirred tank, *Chem. Eng. Sci.* 284 (2024) 119442.
[36] O.P. Klenov, A.S. Noskov, Solid dispersion in the slurry reactor with multiple impellers, *Chem. Eng. J.* 176 (2011) 75–82.
[37] Y.N. Yang, Y.N. Zhou, B. Ouyang, Y.Y. Wu, X.B. Zhang, Z.H. Luo, Influence of thermal runaway in styrene–acrylonitrile bulk copolymerization revealed by computational fluid dynamics modeling, *AIChE J.* 68 (5) (2022) e17645.
[38] Z.M. Kang, L.F. Feng, J.J. Wang, Optimization of a gas–liquid dual-impeller stirred tank based on deep learning with a small data set from CFD simulation, *Ind. Eng. Chem. Res.* 63 (1) (2024) 843–855.
[39] R. Zadghaffari, J.S. Moghaddas, J. Revstedt, Large-eddy simulation of turbulent flow in a stirred tank driven by a Rushton turbine, *Comput. Fluids* 39 (7) (2010) 1183–1190.
[40] N. Lamarque, B. Zoppé, O. Lebaigue, Y. Dolias, M. Bertrand, F. Ducros, Large-eddy simulation of the turbulent free-surface flow in an unbaffled stirred tank reactor, *Chem. Eng. Sci.* 65 (15) (2010) 4307–4322.
[41] B.Q. Liu, M.M. Wang, J.L. Liu, L.Y. Qian, Z.J. Jin, Experimental study on micromixing characteristics of novel large-double-blade impeller, *Chem. Eng. Sci.* 123 (2015) 641–647.
[42] A. Liné, Energy consumption to achieve macromixing revisited, *Chem. Eng. Res. Des.* 108 (2016) 81–87.
[43] U. Schumann, Subgrid scale model for finite difference simulations of turbulent flows in plane channels and annuli, *J. Comput. Phys.* 18 (4) (1975) 376–404.
[44] ANSYS Inc, ANSYS FLUENT Theory Guide Inc. release 19.2, ANSYS Academic, Research, 2019.
[45] J. Smagorinsky, General circulation experiments with the primitive equations, *Mon. Wea. Rev.* 91 (3) (1963) 99–164.
[46] A. Delafosse, J. Morchain, P. Guiraud, A. Liné, Trailing vortices generated by a rushton turbine: assessment of URANS and large eddy simulations, *Chem. Eng. Res. Des.* 87 (4) (2009) 401–411.
[47] T. Henriques, M. Ribeiro, A. Teixeira, L. Castro, L. Antunes, C. Costa-Santos, Nonlinear methods most applied to heart-rate time series: a review, *Entropy* 22 (3) (2020) 309.
[48] N. Sarkar, B.B. Chaudhuri, An efficient differential box-counting approach to compute fractal dimension of image, *IEEE Trans. Syst. Man Cybern.* 24 (1) (1994) 115–120.
[49] P. Grassberger, I. Procaccia, Estimation of the Kolmogorov entropy from a chaotic signal, *Phys. Rev. A* 28 (4) (1983) 2591–2593.
[50] G. Benettin, L. Galgani, J.M. Strelcyn, Kolmogorov entropy and numerical experiments, *Phys. Rev. A* 14 (6) (1976) 2338–2345.
[51] R. Govindarajan, K.C. Sahu, Instabilities in viscosity-stratified flow, *Annu. Rev. Fluid Mech.* 46 (2014) 331–353.
[52] T. Meng, Y. Wang, S. Qin, P.Q. Liu, Y.D. Wang, C.Y. Tao, Z.H. Liu, Complex flow field analysis in multi-shaft stirred reactors: dynamics of wave-vortex coupling revealed by POD and DMD methods, *Chem. Eng. Sci.* 301 (2025) 120753.